

Multi-wavelength elemental contrast absorption imaging

Mac B. Luu,^{1,2,*} Chanh Q. Tran,^{1,2} Benedicta Arhatari,^{1,2}
Eugeniu Balaur,^{1,2} Nirgel Kirby,⁴ Stephen Mudie,⁴ Bao T. Pham,^{1,2}
Nghia T. Vo,⁵ Corey T. Putkunz,^{3,2} Francesco De Carlo,⁶
and Andrew G. Peele^{1,2,4}

¹*Department of Physics, La Trobe University, VIC 3086, Australia*

²*ARC Centre of Excellence for Coherent X-ray Science, Melbourne, Australia*

³*School of Physics, University of Melbourne, VIC 3010, Australia*

⁴*Australian Synchrotron, VIC 3168, Australia*

⁵*Department of Physics, National University of Singapore, 119077, Singapore*

⁶*Advanced Photon Source, Argonne National Laboratory, Illinois 60439, USA*

[*bmluu@students.latrobe.edu.au](mailto:bmluu@students.latrobe.edu.au)

Abstract: We report experimental demonstrations of a quantitative technique for elemental mapping. The technique operates in full-field imaging mode and uses three intensity measurements at energies across an absorption edge of an element of interest to obtain its elemental distribution. The experimental results show that the technique can overcome some limitations in the conventional Absorption Edge Contrast Imaging. The technique allows for an accurate determination of the elemental distribution in a compound sample even at a low level of percentage composition. It is also robust to the choice of energy intervals.

© 2011 Optical Society of America

OCIS codes: (340.0340) X-ray optics; (340.7440) X-ray imaging; (340.6720) Synchrotron radiation.

References and links

1. I. Gurrappa, D. Manova, J. Gerlach, S. Mandl, and B. Rauschenbach, "Influence of nitrogen implantation on the high temperature oxidation of titanium-base alloys," *Surf. Coat. Technol.* **201**, 3536–3546 (2006).
2. J. S. Hou, J. T. Guo, G. X. Yang, L. Z. Zhou, X. Z. Qin, and H. Q. Ye, "The microstructural instability of a hot corrosion resistant superalloy during long-term exposure," *Mater. Sci. Eng., A* **498**, 349–358 (2008).
3. A. S. Yen, R. Gellert, C. Schroder, R. V. Morris, J. F. Bell, A. T. Knudson, B. C. Clark, D. W. Ming, J. A. Crisp, R. E. Arvidson, D. Blaney, J. Bruckner, P. R. Christensen, D. J. DesMarais, P. A. de Souza, T. E. Economou, A. Ghosh, B. C. Hahn, K. E. Herkenhoff, L. A. Haskin, J. A. Hurowitz, B. L. Joliff, J. R. Johnson, G. Klingelhofer, M. B. Madsen, S. M. McLennan, H. Y. McSween, L. Richter, R. Rieder, D. Rodionov, L. Soderblom, S. W. Squyres, N. J. Tosca, A. Wang, M. Wyatt, and J. Zipfel, "An integrated view of the chemistry and mineralogy of martian soils," *Nature* **436**, 49–54 (2005).
4. R. S. Friedman, M. C. McAlpine, D. S. Ricketts, D. Ham, and C. M. Lieber, "Nanotechnology high-speed integrated nanowire circuits," *Nature* **434**, 1085–1085 (2005).
5. H. Rarback, F. Cinotti, C. Jacobsen, J. Kenney, J. Kirz, and R. Rosser, "Elemental analysis using differential absorption techniques," *Biol. Trace Elem. Res.* **13**, 103–113 (1987).
6. S. Laville, L. A. Gizzi, P. Koster, and L. Labate, "Differential absorption imaging for elemental analysis of thin samples using a soft laser-plasma x-ray source," *Nucl. Instrum. Methods Phys. Res. A* **538**, 738–746 (2005).
7. C. Q. Tran, "Multiwavelength elemental contrast phase imaging by the use of dispersion effects," *Phys. Rev. A* **78**, 013839 (2008).
8. J. Miao, P. Charalambous, J. Kirz, and D. Sayre, "Extending the methodology of x-ray crystallography to allow imaging of micrometre-sized non-crystalline specimens," *Nature* **400**, 342–344 (1999).
9. B. Abbey, K. A. Nugent, G. J. Williams, J. N. Clark, A. G. Peele, M. A. Pfeifer, M. de Jonge, and I. McNulty, "Keyhole coherent diffractive imaging," *Nat Phys* **4**, 394–398 (2008).

10. J. N. Clark, G. J. Williams, H. M. Quiney, L. Whitehead, M. D. de Jonge, E. Hanssen, M. Altissimo, K. A. Nugent, and A. G. Peele, "Quantitative phase measurement in coherent diffraction imaging," *Opt. Express* **16**, 3342–3348 (2008).
11. C. T. Putkunz, J. N. Clark, D. J. Vine, G. J. Williams, M. A. Pfeifer, E. Balaur, I. McNulty, K. A. Nugent, and A. G. Peele, "Phase-diverse coherent diffractive imaging: High sensitivity with low dose," *Phys. Rev. Lett.* **106**, 013903 (2011).
12. C. T. Putkunz, M. A. Pfeifer, A. G. Peele, G. J. Williams, H. M. Quiney, B. Abbey, K. A. Nugent, and I. McNulty, "Fresnel coherent diffraction tomography," *Opt. Express* **18**, 11746–11753 (2010).
13. H. M. Quiney, K. A. Nugent, and A. G. Peele, "Iterative image reconstruction algorithms using wave-front intensity and phase variation," *Opt. Lett.* **30**, 1638–1640 (2005).
14. G. J. Williams, H. M. Quiney, B. B. Dhal, C. Q. Tran, K. A. Nugent, A. G. Peele, D. Paterson, and M. D. de Jonge, "Fresnel coherent diffractive imaging," *Phys. Rev. Lett.* **97**, 025506 (2006).
15. B. Arhatari, K. Hannah, E. Balaur, and A. Peele, "Phase imaging using a polychromatic x-ray laboratory source," *Opt. Express* **16**, 19950–19956 (2008).
16. D. Paganin, S. C. Mayo, T. E. Gureyev, P. R. Miller, and S. W. Wilkins, "Simultaneous phase and amplitude extraction from a single defocused image of a homogeneous object," *J. Microsc.* **206**, 33–40 (2002).
17. L. Turner, B. Dhal, J. Hayes, A. Mancuso, K. Nugent, D. Paterson, R. Scholten, C. Tran, and A. Peele, "X-ray phase imaging: Demonstration of extended conditions for homogeneous objects," *Opt. Express* **12**, 2960–2965 (2004).
18. M. B. Luu, B. D. Arhatari, C. Q. Tran, E. Balaur, B. T. Pham, N. T. Vo, B. Chen, C. T. Putkunz, N. Kirby, S. Mudie, and A. G. Peele, "Quantitative phase imaging with polychromatic x-ray sources," *Opt. Express* **19**, 8127–8134 (2011).
19. C. T. Chantler, "Theoretical form factor, attenuation, and scattering tabulation for $z=1-92$ from $e=1-10$ ev to $e=0.4-1.0$ mev," *J. Phys. Chem. Ref. Data* **24**, 71–642 (1995).
20. D. Cookson, N. Kirby, R. Knott, M. Lee, and D. Schultz, "Strategies for data collection and calibration with a pinhole-geometry sabs instrument on a synchrotron beamline," *J. Synchrotron Radiat.* **13**, 440–444 (2006).
21. C. T. Chantler, C. Q. Tran, Z. Barnea, D. Paterson, D. J. Cookson, and D. X. Balaic, "Measurement of the x-ray mass attenuation coefficient of copper using 8.85–20 keV synchrotron radiation," *Phys. Rev. A* **64**, 062506 (2001).
22. J. L. Glover, C. T. Chantler, Z. Barnea, N. A. Rae, C. Q. Tran, D. C. Creagh, D. Paterson, and B. B. Dhal, "Measurements of the x-ray mass-attenuation coefficient and imaginary component of the form factor of copper," *Phys. Rev. A* **78**, 052902 (2008).

1. Introduction

The spatial distribution of individual elements in compound samples are the subject of extensive interest in many fields including materials science and engineering [1,2], mineralogy [3], nano-electronics [4], and biosciences [5]. The use of X-rays, compared to other forms of radiation, in determining the elemental distribution in a compound sample has the advantage of providing three-dimensional information with relatively low radiation damage, high resolution, and high penetration depth. Elemental contrast can be obtained by an analysis of characteristic peaks in the induced fluorescent x-ray spectra, or by measuring transmission through a sample at energies characteristic of various elements. While detectors with both spatial and energy resolution exist, they currently have large pixel sizes and are relatively expensive. To obtain high spatial resolution with elemental sensitivity, typically either a small probe beam is scanned across a sample or the energy of an illuminating beam is varied. Such scanning based techniques can be a laborious process with millions of individual points needing to be scanned.

The most common X-ray full-field imaging technique with elemental mapping capability is the so called Absorption-Edge Contrast Imaging [5,6]. Here the contrast of an element of interest in a compound sample is obtained by normalising the intensities measured at two energies above and below an absorption edge of a given element. This technique can produce useful quantitative data for highly absorbing samples imaged in the near field region. However, several conditions exist under which quantitative data cannot be obtained. In particular, when the energy interval between the two energies is large or when the percentage composition of the element in a compound sample is low.

We recently proposed a technique to obtain spatial distributions of specific elements in a compound sample named Multi-Wavelength Elemental Contrast Phase Imaging [7]. The tech-

nique involves a normalisation of intensities measured at three different energies across an absorption edge of the element of interest. This technique can be applied to most existing x-ray phase retrieval imaging techniques such as Coherent Diffractive Imaging (CDI) [8, 9], Fresnel Coherent Diffractive Imaging (FCDI) [10–14], Transport of Intensity Equation (TIE) [15, 16], or Contrast Transfer Function (CTF) [17, 18].

In this paper, we apply the idea of the normalization process using three energies made in [7] to the absorption domain. The technique is called Multi-Wavelength Elemental Contrast Absorption Imaging (MWECAI) and is particularly useful for absorbing samples. We show that the MWECAI technique can achieve quantitative elemental specific information about compound samples, even at low percentage compositions and where large energy intervals are used.

2. The Multi-wavelength elemental contrast absorption technique

Consider three spatially resolved measurements of intensity transmitted through a sample at energies, $E - \Delta E$, E , and $E + \Delta E$ in the vicinity of an absorption edge of an element of interest. Assume that the absorption edge is in between E and $E + \Delta E$. It should be noted that the theoretical derivation described in this section is also valid when the absorption edge is in between $E - \Delta E$ and E . The absorption of the compound sample at an energy, E , can be defined as

$$A_E(\mathbf{r}) = -\ln \left[\frac{I_E(\mathbf{r})}{I_{0,E}(\mathbf{r})} \right] = \left[\left(\frac{\mu}{\rho} \right)_{e,E} \rho_e T_e(\mathbf{r}) + \sum_j \left(\frac{\mu}{\rho} \right)_{j,E} \rho_j T_j(\mathbf{r}) \right], \quad (1)$$

where $\mathbf{r} \equiv (x, y)$ is the 2D position vector in the transverse plane; $I_{0,E}(\mathbf{r})$ and $I_E(\mathbf{r})$ are the incident and attenuated intensities at energy E , in that order; ρ_e , $\left(\frac{\mu}{\rho} \right)_{e,E}$, and $T_e(\mathbf{r})$ are the volume density, the mass attenuation coefficient at energy E , and the thickness of the element of interest. The sum over the subscript j is for all elements other than the element of interest with in the sample. There is an inherent ambiguity between the density and the thickness of an element in a compound sample. Generally, the product is the quantity of interest although we may resolve the components into bulk density and effective thickness or reduced density and actual thickness depending on the type of sample.

The normalized Multi-Wavelength Elemental Contrast Absorption (MWECAI) can be defined as

$$\Delta_{MWECAI}(\mathbf{r}) \equiv A_{E+\Delta E}(\mathbf{r}) + A_{E-\Delta E}(\mathbf{r}) - 2A_E(\mathbf{r}), \quad (2)$$

and the corresponding normalised mass attenuation coefficients are

$$\Delta \left(\frac{\mu}{\rho} \right)_e \equiv \left(\frac{\mu}{\rho} \right)_{e,E+\Delta E} + \left(\frac{\mu}{\rho} \right)_{e,E-\Delta E} - 2 \left(\frac{\mu}{\rho} \right)_{e,E},$$

and

$$\Delta \left(\frac{\mu}{\rho} \right)_j \equiv \left(\frac{\mu}{\rho} \right)_{j,E+\Delta E} + \left(\frac{\mu}{\rho} \right)_{j,E-\Delta E} - 2 \left(\frac{\mu}{\rho} \right)_{j,E}.$$

The normalisation in Eq. (2) can be expressed as

$$\begin{aligned} \Delta_{MWECAI}(\mathbf{r}) &= [\rho_e T_e(\mathbf{r})] \Delta \left(\frac{\mu}{\rho} \right)_e + \sum_j [\rho_j T_j(\mathbf{r})] \Delta \left(\frac{\mu}{\rho} \right)_j \\ &= \Delta A_e(\mathbf{r}) + \Delta A_{residue}(\mathbf{r}), \end{aligned} \quad (3)$$

where $\Delta A_e(\mathbf{r})$ represents the contrast due to the presence of the element of interest and $\Delta A_{residue}$ represents the net residue term due to the presence of all other elements in a sample. However,

if the absorption edges of all elements in the sample, other than the element of interest, are not in the vicinity of the small energy interval $[E - \Delta E, E + \Delta E]$ then their attenuation coefficients, to a good approximation, vary linearly within the energy interval. Under this condition, $\Delta\left(\frac{\mu}{\rho}\right)_j$ approaches zero and, as a consequence, the normalized absorption is a good approximation of the distribution of the element of interest in the sample,

$$\Delta_{MWECA}A(\mathbf{r}) \approx \Delta A_e(\mathbf{r}). \quad (4)$$

Thus the projected thickness of the element can be approximately obtained as

$$T_{e,MWECA}(\mathbf{r}) \approx \frac{\Delta_{MWECA}A(\mathbf{r})}{\rho_e \Delta\left(\frac{\mu}{\rho}\right)_e}. \quad (5)$$

The percentage approximation error involved in using Eq. (4) is

$$Err_{MWECA}(\mathbf{r}) \equiv \frac{\Delta A_{residue}(\mathbf{r})}{\Delta A_e(\mathbf{r})} \times 100\%, \quad (6)$$

which is small. In regions where the element of interest is not present, the normalised absorption is expected to be zero and the error should be better expressed as a simple residue.

In order to highlight the sensitivity of the technique, we compare Eq. (3) and (6) with their equivalents using the conventional absorption edge contrast technique [5, 6]. Defining the normalized absorption in the conventional absorption edge contrast technique as

$$\Delta_{conv}A(\mathbf{r}) \equiv A_{E+\Delta E}(\mathbf{r}) - A_E(\mathbf{r}), \quad (7)$$

the corresponding normalized mass attenuation coefficients are

$$\Delta_{conv}\left(\frac{\mu}{\rho}\right)_e \equiv \left(\frac{\mu}{\rho}\right)_{e,E+\Delta E} - \left(\frac{\mu}{\rho}\right)_{e,E},$$

and

$$\Delta_{conv}\left(\frac{\mu}{\rho}\right)_j \equiv \left(\frac{\mu}{\rho}\right)_{j,E+\Delta E} - \left(\frac{\mu}{\rho}\right)_{j,E}.$$

Using Eq. (1) we can rewrite Eq. (7) as

$$\begin{aligned} \Delta_{conv}A(\mathbf{r}) &= [\rho_e T_e(\mathbf{r})] \Delta_{conv}\left(\frac{\mu}{\rho}\right)_e + \sum_j [\rho_j T_j(\mathbf{r})] \Delta_{conv}\left(\frac{\mu}{\rho}\right)_j \\ &= \Delta_{conv}A_e(\mathbf{r}) + \Delta_{conv}A_{residue}(\mathbf{r}). \end{aligned} \quad (8)$$

The conventional technique relies on the assumption that the term $\Delta_{conv}A_{residue}(\mathbf{r})$ is small except for cases where $\rho_e T_e(\mathbf{r}) \ll \rho_j T_j(\mathbf{r})$ so that

$$\Delta_{conv}A(\mathbf{r}) \approx \Delta_{conv}A_e(\mathbf{r}), \quad (9)$$

hence the thickness of the element can be obtained as

$$T_{e,conv}(\mathbf{r}) = \frac{\Delta_{conv}A(\mathbf{r})}{\rho_e \Delta\left(\frac{\mu}{\rho}\right)_e}, \quad (10)$$

and the percentage approximation error involved in Eq. (9) is therefore:

$$Err_{conv}(\mathbf{r}) = \frac{\Delta_{conv}A_{residue}(\mathbf{r})}{\Delta_{conv}A_e(\mathbf{r})} \times 100\%. \quad (11)$$

To first order, $\Delta_{conv}\left(\frac{\mu}{\rho}\right)_e$ is the difference in the mass attenuation coefficients across the absorption edge of the element of interest and $\Delta_{conv}\left(\frac{\mu}{\rho}\right)_j$ is proportional to the energy separation ΔE . Since ΔE has a practical lower bound of a few 10 eVs, $Err_{conv}(\mathbf{r})$ can be significant when $\sum_j \rho_j T_j(\mathbf{r}) \geq \rho_e T_e(\mathbf{r})$.

The percentage composition of the element of interest in the compound sample can be defined as

$$C(\mathbf{r}) = \frac{\rho_e T_e(\mathbf{r})}{\rho_e T_e(\mathbf{r}) + \sum_j \rho_j T_j(\mathbf{r})} \times 100\%. \quad (12)$$

The effect of C and ΔE on the approximation errors for the conventional and the MWECAI techniques can be modelled. Figure 1 shows the prediction of the approximation errors Err_{MWECAI} and Err_{conv} as defined in Eq. (6) and Eq. (11), respectively, for a sample consisting of copper (the element of interest) and gold (other elements). While differences are to be expected with varying choices for elements and energy separation we find that the general trend of the curve is generic to a very wide range of choices. Compared to the error involved using the conventional technique (Fig. 1(b)), the error involved in using the MWECAI technique (Fig. 1(a)) is small over wide ranges of both the percentage compositions for the element of interest and the energy separations. In fact, in the absence of statistical noise, Err_{MWECAI} is about two orders of magnitude less than Err_{conv} . Figure 2 shows a 1D comparison of the errors using data extracted from Fig. 1(a) and Fig. 1(b) at $\Delta E = 60$ eV. It is obvious from Fig. 2 that even at low levels of percentage composition ($\sim 1\%$) the MWECAI technique can still achieve good quantitative results ($Err_{MWECAI} < 1\%$), whereas the conventional technique becomes seriously limited ($Err_{conv} \approx 120\%$). The calculations shown in Fig. 1 and Fig. 2 are based on known values for the mass attenuation coefficients [19].

3. Experimental demonstrations

We demonstrate the advantage of the technique using results from two experiments. The first experiment aimed to demonstrate the sensitivity of the MWECAI technique as a function of the percentage composition of an element of interest in a compound sample. The second experiment aimed to investigate the sensitivity of the MWECAI technique as a function of the energy gap, ΔE , between the measurements.

3.1. Percentage approximation errors as functions of the percentage composition of an element of interest in an compound sample

The first experiment was conducted at the SAXS-WAXS beamline of the Australian Synchrotron. We used two compound samples, each consisted of two partially overlapping layers of Cu and Au of similar lateral dimension $100 \mu m \times 200 \mu m$ though the thickness varied between the samples. For the first sample (Fig. 3(a)), the thicknesses of both the Cu and the Au layers were 100 nm . For the second sample (Fig. 4(a)), the thicknesses of the Cu and the Au layers were 100 nm and $1.8 \mu m$, in that order. The nominal bulk densities of Cu and Au are 8.94 g cm^{-3} and 18.85 g cm^{-3} , respectively [19]. The percentage composition of Cu in the overlapping regions of the samples calculated using Eq. (12) is 32.17% for first sample and 2.57% for the second sample.

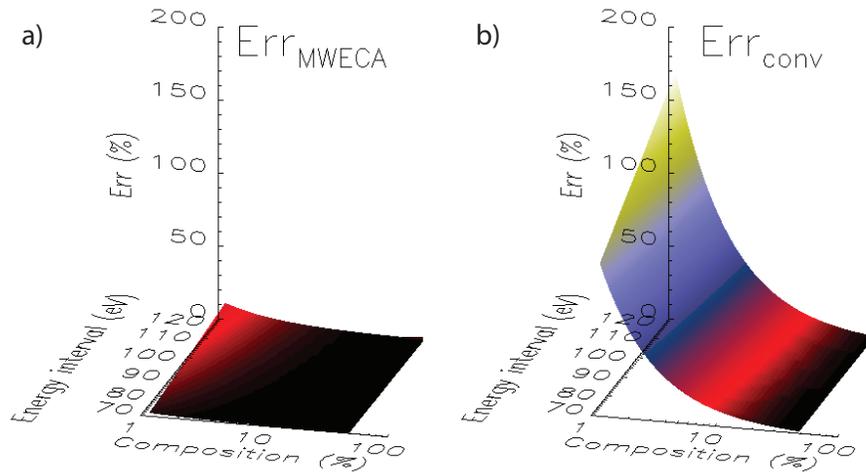


Fig. 1. (a) Percentage approximation error, Err_{MWECA} ; and (b) percentage approximation error, Err_{conv} as functions of the percentage composition of the element of interest, and energy interval.

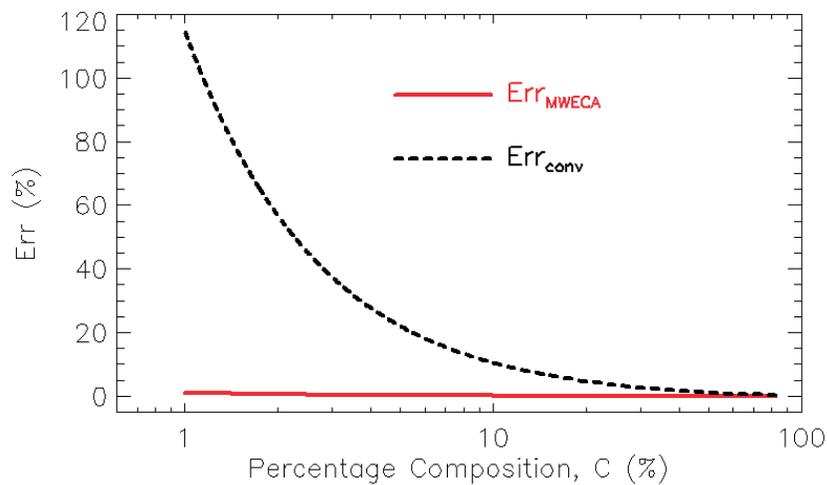


Fig. 2. Line profiles of the percentage approximation errors shown in Fig. 1(a) and Fig. 1(b), which are 1D distributions of $Err_{MWECA}(\mathbf{r})$, and $Err_{conv}(\mathbf{r})$ as functions of percentage composition, $C(\mathbf{r})$ of the element of interest.

A CCD detector of 2048×2048 pixels coupled with a scintillator was used to measure the intensity at a propagation distance of $120 \text{ mm} \pm 2 \text{ mm}$ from the samples. This propagation distance was the shortest possible due to the geometry of the sample stage and the detector used in the experiment.

The physical pixel size of the CCD was $13.5 \mu\text{m}$, and with the use of a 10X magnification lens, the effective pixel size was $1.35 \mu\text{m}$. This was confirmed by calibrating the displacement of a feature in the measured images of the sample against the positions of the detector stage.

The copper K-edge was calibrated to be $8985 \text{ eV} \pm 2 \text{ eV}$ relative to the energy determined by the angular position of the beamline monochromator [20]. Two ion chambers were placed

upstream and downstream of a Cu foil. These chambers were used to record the incident and transmitted intensity of the x-ray beam. The energy was scanned in a 1 eV step from in 8.75 keV to 9.15 keV to calibrate the K-edge of Cu.

Intensity measurements were carried out at 8910 eV, 8970 eV, and 9030 eV. The measurements were repeated 50 times to reduce statistical noise. Figure 3(b) and Fig. 4(b) show typical intensities as measured at 9030 eV of the first and the second samples, in that order.

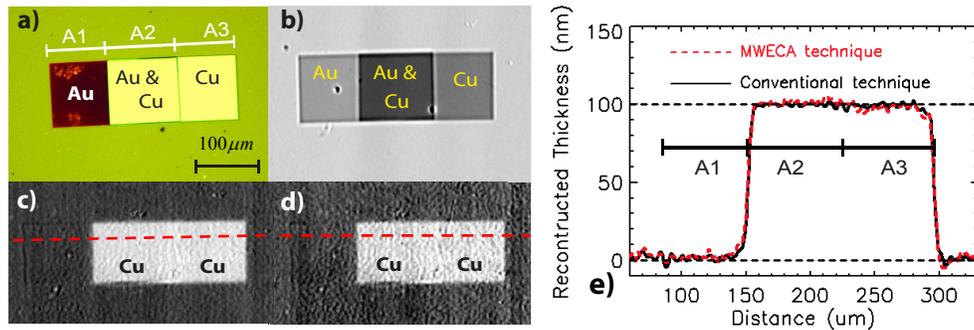


Fig. 3. (a) The first sample consists of 100 nm thick Au and Cu in each of the regions labeled; (b) Intensity measured at an energy of 9030 eV. The distribution of Cu produced: (c) by the conventional technique; and (d) by the MWECAI technique; (e) the plots along the dashed lines in (c) and (d) show the comparison between the conventional technique and our technique.

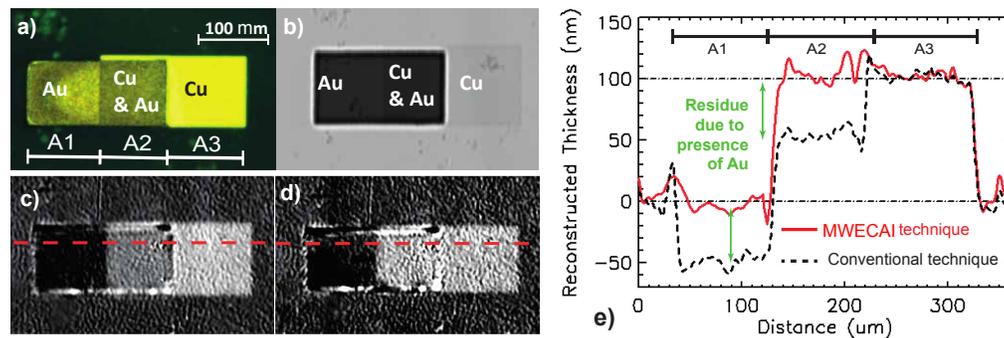


Fig. 4. (a) The second sample consists of a layer of Au with a thickness of 1.8 μm, and a layer of Cu with a thickness of 100 nm; (b) Intensity measured at an energy of 9030 eV. The distribution of Cu produced: (c) by the conventional technique; and (d) by our technique; (e) the plots along the dashed lines in (c) and (d) show the comparison between the conventional technique and our technique.

For both samples, the contrast due to the presence of Cu was determined by applying both the MWECAI (Eq.(3)) and the conventional techniques (Eq.(8)). Assuming bulk density in Cu, the projected thicknesses, $T_{Cu}(\mathbf{r})$, of Cu in the two samples was determined by using Eq. (5) and Eq. (10) for the MWECAI and the conventional techniques, respectively. The 2D results for the projected thickness for both samples processed using of the conventional technique are shown in Fig. 3(c) and Fig. 4(c). The corresponding results for the MWECAI technique are shown in Fig. 3(d) and Fig. 4(d). One-dimensional comparisons of the projected thicknesses

Table 1. Thickness of Cu obtained by the two techniques for the two samples for the regions labeled in Fig. 3 and Fig. 4

Samples	Average thickness	$r \in A1$	$r \in A2$	$r \in A3$
Sample 1	$T_{e,conv}$	2 nm \pm 2 nm	100 nm \pm 2 nm	100 nm \pm 2 nm
	$T_{e,MWECA}$	2 nm \pm 2 nm	100 nm \pm 2 nm	100 nm \pm 2 nm
Sample 2	$T_{e,conv}$	-48 nm \pm 5 nm	54 nm \pm 5 nm	102 nm \pm 4 nm
	$T_{e,MWECA}$	-4 nm \pm 5 nm	105 nm \pm 8 nm	102 nm \pm 4 nm

obtained using both techniques are shown in Fig. 3(e) and Fig. 4(e), for the first and the second samples, in that order. The 1D data were extracted along the dashed-line shown in panels (c) and (d) of Fig. 3 and Fig. 4.

The uncertainty of the local projected thickness of copper (Fig. 3 and Fig. 4) consists of several components which include accuracy of the tabulated values for (μ/ρ) and signal to noise in measurements. The error term due to signal to noise in the MWECAI technique will be larger than that in the conventional method as more intensity measurements are used to construct the result in the MWECAI technique. The uncertainty involved in the normalization process of the MWECAI technique is about $\sqrt{2}$ of that of the conventional technique. To better compare the accuracy of the two methods (rather than the uncertainty in their result) the plots in Fig. 3(e) and Fig. 4(e) were the profiles along the dashed-lines (in Fig. 3(c) and Fig. 3(d), and Fig. 4(c), Fig. 4(d) averaged from the bottom-edge to the top-edge of the entire samples. Therefore the noise in the plots (shown in Fig. 3(e) and Fig. 4(e)) is small as the signal to noise is improved by the averages.

The average thicknesses of Cu in regions (A1, A2 and A3) is shown in Table 1. The uncertainties in the average thicknesses of copper listed in table 1 were represented by the standard deviations of the local thickness of copper in the appropriate regions calculated from the plots in Fig. 3(e) and Fig. 4(e).

As shown in Fig. 3(e) and Fig. 4(e), both techniques achieved accurate determination of the projected thicknesses of Cu in the regions where the percentage composition of Cu is high (region A3 of both samples and region A2 of the first sample). This thickness was verified using Atomic Force Microscopy and was also consistent with nominal thickness predicted using the fabrication parameters. In fact, both techniques appear to be accurate in region A1 of Sample 1 where background noise dominates as there is no element of interest and very little residue elements.

When the percentage composition of Cu is low (region A1 of both samples and region A2 of the second sample), we expect only the MWECAI technique to be accurate. Our expectation is true in regions A1 and A2 of the second sample. In fact, in region A2 of Sample 2, the conventional technique becomes significantly limited ($Err_{conv}(\mathbf{A}_2) \approx 46\%$). In contrast, the error in the MWECAI technique is negligible ($Err_{MWECA}(\mathbf{A}_2) \approx 2\%$), which is similar to the noise level in the normalised absorption. In addition, in region A1 of Sample 2 the conventional technique produces a non physical result for the normalised absorption and hence the projected thickness. The effectiveness of both techniques as discussed in these cases is consistent with the prediction shown in Fig. 2.

We note that diffraction fringes can be observed at the edges of the sample in the measured intensities as shown in Fig. 3(b) and Fig. 4(b). However, these fringes are canceled out after the normalisations using either the conventional or the MWECAI techniques as shown in Fig. 3(c), Fig. 4(c) and Fig. 3(d), Fig. 4(d) respectively. The cancellation of these fringes allows for the application of the absorption based technique described in this work. One could also use a phase-based technique which can handle absorbing samples to analyse the results. However, a

detailed discussion about a phase-base analysis is beyond the scope of this work.

Finally, it should be noted that the mass attenuation coefficients (μ/ρ) at the three energies were linearly interpolated using tabulated values from a NIST database [19]. The tabulated (μ/ρ) were calculated using independent particle and isolated atom approximations and therefore did not include atomic fine structure. This leads to a small error (a few percent) in the final result of the projected thickness of the Copper. This could be avoided by using an experimentally determined set of (μ/ρ) which is calibrated on both absorption and energy scales such as [21,22].

3.2. Percentage approximation errors as functions of energy interval

The MWECAI technique also overcomes a limitation of the conventional technique in that it is robust to using enough large energy intervals.

The second experiment was conducted at Beam-line 2-BM of the Advanced Photon Source. The attenuated and incident intensities were measured with and without a compound sample intercepting the beam. The detector was a CCD with 2048×2048 pixels coupled with scintillator, and located at 7 mm behind the sample plane. The CCD pixel size was calibrated against the positions recorded from its positioning motors to be $1.5 \mu\text{m}$. The sample was constructed using two metal meshes overlaying each other. The metal meshes are arrays of square cells made of Cu and Ni respectively. The hole square cells are $97 \mu\text{m}$, and each metal bar is about $10 \mu\text{m}$ thick and $28 \mu\text{m}$ wide. The density of Ni is 8.876 gcm^{-3} and the density of Cu is 8.940 gcm^{-3} [19]. Therefore, the percentage composition of Cu in this sample is 50.2%.

The incident beam was monochromatised by a Si (111) monochromator, and was tuned to energies across the Cu K-edge. The position of the Cu K-edge was determined to be $8980 \pm 2 \text{ eV}$ by a similar setup to that used in the previous experiment. The measured absorption edge is shown in Fig. 5.

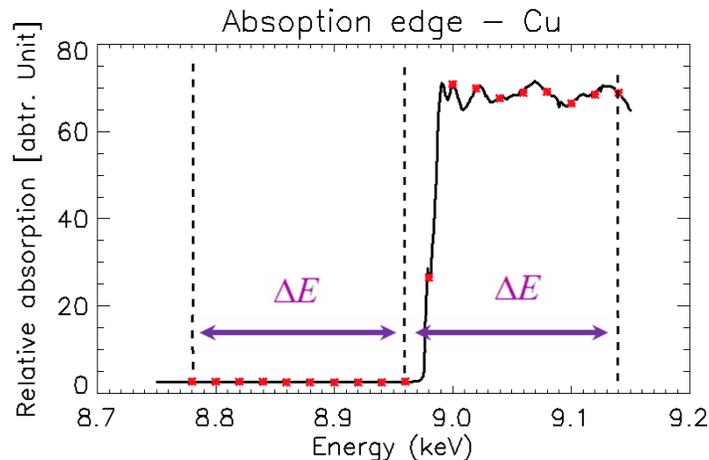


Fig. 5. Left image shows an measured absorption edge of Cu. The red-star-symbols indicate energies at which the intensity measurements were measured. The dashed lines shows a particular set of 3 intensity measurements for the MWECAI technique; here 8780 eV, 8960 eV and 9140 eV. The two intensity measurements at energies of 8960 eV and 9140 eV are used for the conventional technique.

Intensity measurements were carried out at twenty energies ranging from 8760 eV to 9140 eV (i.e. $8760 \text{ eV} + m \times 20 \text{ eV}$, where $m = 1..20$). In other words, the energy separation between any

two adjacent intensity measurements was 20 eV. 20 red-star-points indicated on the measured absorption curve is shown Fig. 5. Those intensity measurements were repeated three times to reduce statistical noise. At each energy, the normalized absorption was calculated from the measured intensities using Eq. (1) and the results at the energies of 8960 eV and 9140 eV are shown in Fig. 6(a) and Fig. 6(b), in that order.

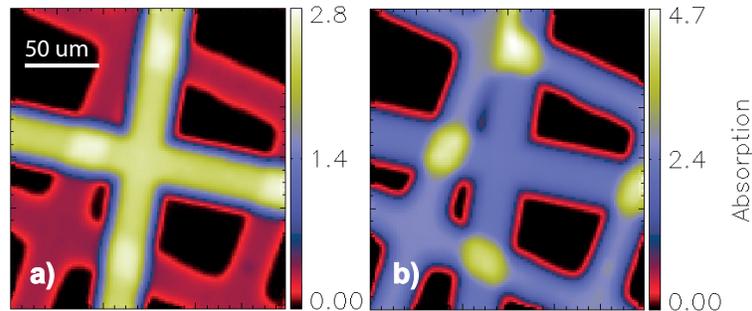


Fig. 6. (a) Net absorption functions of the compound sample calculated from corresponding intensities measured at energies of 8960 eV; and (b) 9140 eV.

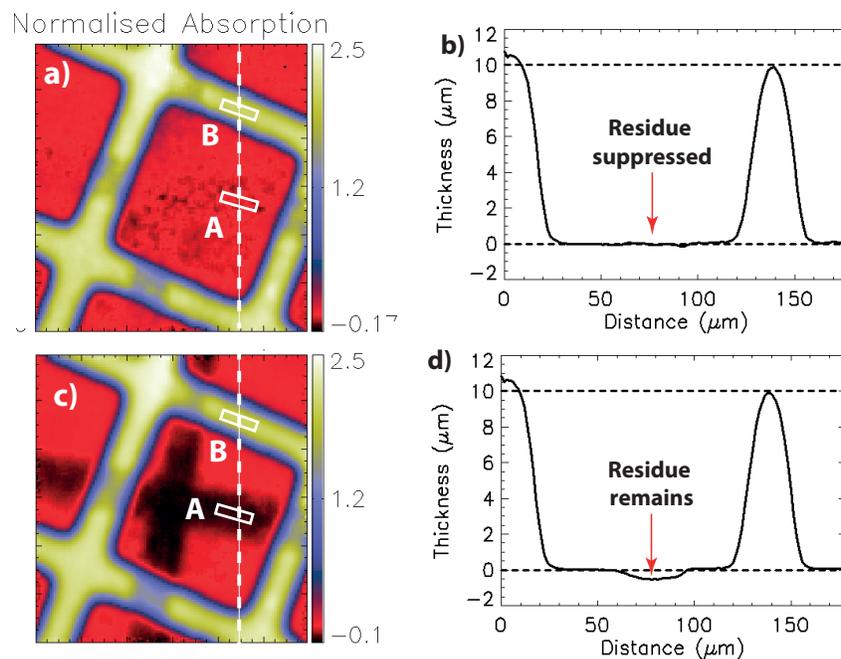


Fig. 7. (a) Projected thickness of Cu as obtained by the MWECAI technique; and (c) the conventional technique. (b) The line plots along the dashed-lines shown in (a) and (c) are the thicknesses obtained by the MWECAI; and (d) the conventional techniques, respectively.

The projected thicknesses of Cu were obtained by applying the MWECAI and the conventional Absorption Edge Contrast techniques as discussed previously and the results are shown in Fig. 7(a) and Fig. 7(c), in that order. In this results we have averaged the measured intensity

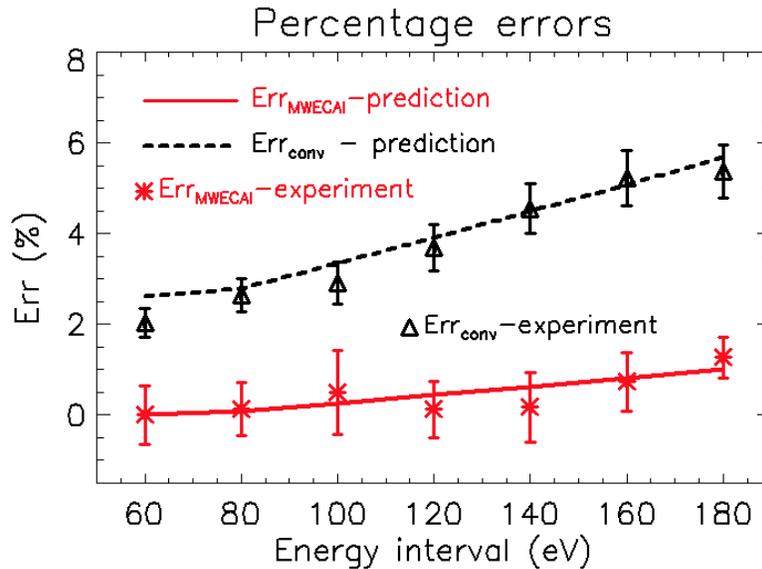


Fig. 8. Percentage approximation error, $Err_{MWECAI}(\mathbf{r})$ and $Err_{conv}(\mathbf{r})$ as functions of energy interval, ΔE . The horizontal axis represents the energy intervals. The vertical axis represents residue due to the presence of Ni remaining in the normalisation. The prediction curves were calculated using tabulated data from the NIST data [19].

resulting in a net spatial resolution of $6 \mu\text{m}$. The 1D profiles along the dashed lines of Fig. 7(a) and Fig. 7(c) are shown in Fig. 7(b) and Fig. 7(d), respectively. It is observed from these figures that, while the residue of Ni is removed cleanly using the MWECAI technique (Fig. 7(b)), there is a significant residue remaining after the normalisation process using the conventional technique as shown in the central region of Fig. 7(d).

The effect of the energy separation on the percentage approximation errors using the two techniques was quantified by comparing the values of Err_{conv} and Err_{MWECAI} against the energy separations. In the region of Cu and Ni overlap the net transmission was too low to provide any useful data. However we can still evaluate the effectiveness of the normalisation techniques by calculating the percentage approximation errors using the residue of Ni ($\Delta A_{residue}$ in region A) and the normalised absorption of Cu (ΔA_e in region B). Those values were averaged within the regions and they are indicated as small rectangles A and B in Fig. 7(a) and Fig. 7(c). The experimental results are also shown in Fig. 8, where the mean energy E was fixed at 8960 eV and the experimental error bars were estimated as the standard deviation of the ratios obtained within the averaging regions. The corresponding theoretical predictions are also calculated based on known values for mass attenuation coefficients for Cu and Ni [19], as shown in Fig. 8. It is observed that there is excellent agreement between the experimental results and the theoretical prediction. In particular from Fig. 8, the percentage error for the conventional technique increases significantly when the energy interval increases, whereas that for the MWECAI technique remains relatively small. The discontinuity observed at 80 eV in Fig. 8 was due to a discontinuity in the tabulated values of the mass attenuation coefficient (μ/ρ) [19].

In addition, despite the high percentage composition of Cu in this sample ($\sim 50.2\%$), the MWECAI technique still achieves a much better quantitative reconstruction of the thickness of Cu over the entire range of energy separation. This result confirms that the MWECAI technique is robust to the choice of energy intervals. This advantage could be explored further to

investigate the possibility of applying the MWECAI to polychromatic imaging.

4. Conclusion

We have experimentally demonstrated the MWECAI technique in determining the spatial distribution of Cu in compound samples. The technique operates in full-field imaging mode and therefore is much simpler and more effective than scanning based techniques such as STXM fluorescence microscopy. Our technique can achieve correct quantitative reconstruction of the projected thickness (ρT) of an element of interest in a compound sample even at a low level of a few percentage composition or large energy separations (~ 100 eV).

The technique has particular application where transmission measurements are required and where the incident energy may be readily varied, such as at a synchrotron source.

Acknowledgement

The authors acknowledge the support of the Australian Research Council through the Centre of Excellence for Coherent X-ray Science. The authors acknowledge the uses of the Advanced Photon Source at Argonne National Laboratory supported by the U. S. Department of Energy, Office of Science, Office of Basic Energy Sciences, under Contract No. DE-AC02-06CH11357. We acknowledge travel funding provided by the Australian Synchrotron Research Program (ASRP) managed by the Australian Synchrotron and funded by the Australian Government. This research was undertaken on the SAXS/WAXS beamline at the Australian Synchrotron, Victoria, Australia and on the 2BM beam line at the Advanced Photon Source, Argonne National Laboratory, US. The authors acknowledge the supports all the SAXS/WAXS and the 2BM beamline scientists. The authors also acknowledge Aidan Carroll for his support on spelling and grammar corrections of this paper.